LETTERS

Doping semiconductor nanocrystals

Steven C. Erwin[1]*, Lijun Zu[2]*, Michael I. Haftel[1], Alexander L. Efros[1], Thomas A. Kennedy[1] & David J. Norris[2]

Doping—the intentional introduction of impurities into a material—is fundamental to controlling the properties of bulk semiconductors. This has stimulated similar efforts to dope semiconductor nanocrystals[1–4]. Despite some successes[5–11], many of these efforts have failed, for reasons that remain unclear. For example, Mn can be incorporated into nanocrystals of CdS and ZnSe (refs 7–9), but not into CdSe (ref. 12)—despite comparable bulk solubilities of near 50 per cent. These difficulties, which have hindered development of new nanocrystalline materials[13–15], are often attributed to 'self-purification', an allegedly intrinsic mechanism whereby impurities are expelled. Here we show instead that the underlying mechanism that controls doping is the initial adsorption of impurities on the nanocrystal surface during growth. We find that adsorption—and therefore doping efficiency—is determined by three main factors: surface morphology, nanocrystal shape, and surfactants in the growth solution. Calculated Mn adsorption energies and equilibrium shapes for several nanocrystals lead to specific doping predictions. These are confirmed by measuring how the Mn concentration in ZnSe varies with nanocrystal size and shape. Finally, we use our predictions to incorporate Mn into previously undopable CdSe nanocrystals. This success establishes that earlier difficulties with doping are not intrinsic, and suggests that a variety of doped nanocrystals—for applications from solar cells[16] to spintronics[17]—can be anticipated.

When a macroscopic semiconductor crystal is grown under conditions of thermal equilibrium, impurity atoms can be incorporated up to their solid solubility limit—as much as 50% or more for Mn in II–VI semiconductors[18]. This thermodynamic limit is completely determined by the Gibbs free energy (approximately equal to the impurity formation energy) and the growth temperature. For semiconductor nanocrystals—which are typically grown using colloidal synthesis—the impurity concentrations attained in experiments are much lower than expected from this limit[7,8], and for some materials are even zero[12]. The likely reason is that thermal equilibrium, which requires facile diffusion, may be far from realized. Indeed, at the temperatures used in colloidal growth, typically around 300 °C, diffusion of Mn in II–VI semiconductors is negligible; for example, the diffusion length of Mn in CdTe after 1 h at this temperature is only 1–3 Å (ref. 19). This suggests that thermal equilibrium is an inappropriate starting point for describing doping in nanocrystals.

We propose instead a simple model of doping based on kinetics. Specifically, we hypothesize that impurities are incorporated into a nanocrystal only if they can bind to its surface for a residence time comparable to the reciprocal growth rate. In this model, impurity diffusion within the nanocrystal plays no role, even though diffusion (of both impurities and host atoms) on the nanocrystal surface may occur. To explore the consequences of the model, we make two reasonable assumptions: first, that the nanocrystal surface consists of well-defined facets (as observed experimentally[20,21]), and second, that the binding energy of an impurity adsorbed on a given facet determines its residence time. Figure 1 shows theoretical binding energies, calculated using density-functional theory[22,23] (see Methods), for Mn adsorbed on the three most important facets of six representative II–VI and IV–VI semiconductors. Of particular interest are the binding energies on the (001) surfaces of crystals with the zinc-blende structure. These energies are strikingly larger, by factors of 2–10, than on the other two zinc-blende orientations, or on any facet of crystals with the wurtzite or rock-salt structures. The origin of this difference is the unique morphology of (001) surfaces of zinc-blende (and diamond) crystals, which typically consists of various arrangements of anion dimers. These dimers provide very stable binding sites that are absent from the (110) and (111) surfaces of zinc-blende crystals, and from all surfaces of wurtzite and rock-salt crystals. The resulting strong binding indicates that the (001) facets of zinc-blende nanocrystals play a special role in the doping process.

Indeed, a survey of the experimental literature reveals that all of the nanocrystals that have been successfully doped with individual Mn atoms (ZnS, ZnSe, CdS) exhibit the zinc-blende crystal structure[5–9]. In contrast, those that have the wurtzite (CdSe) or rock-salt structure (PbS, PbSe) have either not been successfully doped, or have required polychalcogenide precursors to incorporate Mn in cluster form as a prebonded Se–Mn complex (a technique beyond the scope of our model)[10,12,24]. The correspondence between these earlier results and our adsorption findings strongly suggests a new view of doping: that individual Mn impurities are most easily incorporated in nanocrystals with the zinc-blende crystal structure, by adsorbing on their (001) facets.

To explore in detail the consequences of this view, we begin by developing a model describing how doping efficiency varies over the range of possible nanocrystal shapes. For nanocrystals having the zinc-blende structure and more than one facet orientation, we assume that only the regions bounded by (001) facets can be doped. Hence, the dopable fraction, f, of the nanocrystal volume is given by the relative surface area of its (001) facets. For nanocrystals grown out of equilibrium, f can only be determined directly from knowledge of the nanocrystal shape. However, for a nanocrystal that assumes its equilibrium crystal shape, f can be determined analytically from the surface energies, E, of its possible facets. As Fig. 2 shows, (001) facets will be present (that is, $f > 0$) only if these energies satisfy $E_{110}/E_{100} > 1/\sqrt{2}$ and $E_{111}/E_{100} > 1/\sqrt{3}$. The limiting case of a nanocrystal consisting entirely of (001) facets (that is, $f = 1$) occurs when $E_{110}/E_{100} = \sqrt{2}$ and $E_{111}/E_{100} = \sqrt{3}$. For intermediate surface-energy ratios, the stable facets and relative areas shown in Fig. 2 were determined by finding the crystal shape that minimizes the total surface energy within the constraint of fixed volume.

To predict the value of f for a specific material, we must calculate absolute surface energies for all the facet orientations considered. For

[1]Naval Research Laboratory, Washington DC 20375, USA. [2]Department of Chemical Engineering & Materials Science, University of Minnesota, Minneapolis, Minnesota 55455, USA.
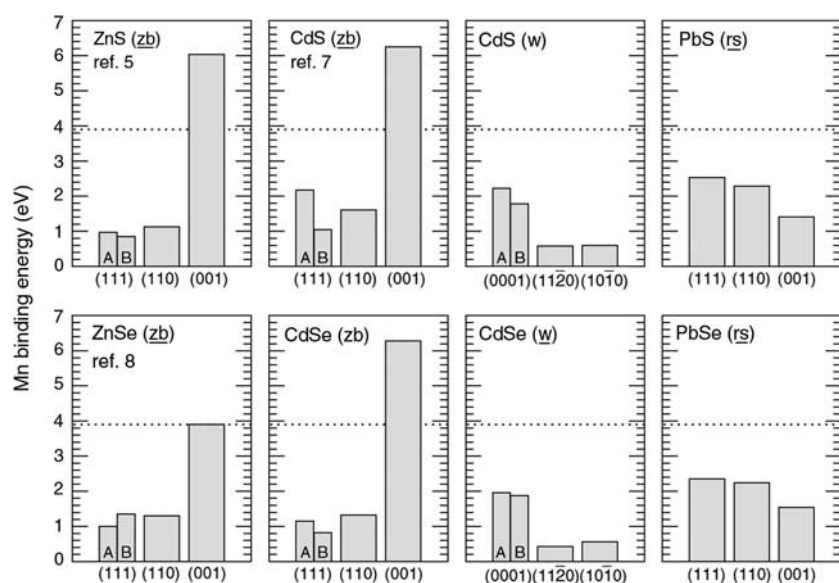*These authors contributed equally to this work.

Figure 1 | Theoretical binding energies for individual Mn adsorbates on various semiconductor surfaces. The crystal structure of these semiconductors is either zinc blende (zb), wurtzite (w) or rock salt (rs); the most commonly occurring structure in nanocrystal form is underlined. Binding energies were calculated for reconstructed surfaces (see Methods) of the three most common crystallographic orientations; 'A' and 'B' denote inequivalent terminations of surfaces having the same orientation. For comparison, the binding energy per atom of bulk crystalline Mn is shown by the dotted line. Nanocrystals that have been successfully doped with individual Mn are indicated by appropriate citations.

a compound semiconductor, it is important to note that the surface energy is not uniquely defined, but rather depends on the relative concentration of its constituents through their chemical potentials. This raises the interesting possibility of controlling the nanocrystal shape—and thereby its doping efficiency—by varying these concentrations. For the example of ZnSe, by assuming specific surface morphologies (for simplicity, we have used reconstructions based on bulk crystal surfaces; see Methods) we can predict the allowed range of expected equilibrium crystal shapes at zero temperature as the chemical potentials are varied between the Zn-rich and Se-rich limits. As shown in Fig. 2, the predicted range of f is between zero (Zn-rich) and 0.3 (Se-rich). Of course, at finite temperatures, this geometrical construction must be modified to account for thermal rounding and related effects[25], but in principle f can still be sensibly defined.

To test these predictions experimentally, we prepared Mn-doped ZnSe nanocrystals with diameters in the range 25–50 Å (ref. 8). After initial nucleation at 310 °C, nanocrystal growth proceeded at temperatures in the range 260–300 °C, using two different Mn:Zn ratios in solution (atomic ratios, 0.05 and 0.025). For each, several different Se:Zn ratios were used (in the range 0.5–4.0) to investigate how doping efficiency varied with Se chemical potential.

Figure 2 | Equilibrium crystal shape for cubic systems, as determined by the ratios of their surface energies. a, Phase diagram specifying which facets are present in the equilibrium crystal shape. **b,** Relative surface area of (111), (001) and (110) facets (red, green and blue shading, respectively) in the equilibrium crystal shape. Contours of constant relative (001) facet area are shown; this quantity gives the relative doping fraction, f, for nanocrystals having the zinc-blende structure. Numbers on the right label the contours. For ZnSe, calculated surface energies lead to the indicated range of equilibrium crystal shapes; the extremal crystal shapes in the Se- and Zn-rich limits are shown at right.

In large nanocrystals, Mn incorporation can be measured directly, using inductively coupled plasma atomic emission spectroscopy (ICP). For nanocrystals of diameter 50 Å grown with Se:Zn = 1, we measured the concentrations of incorporated Mn to be 0.23% (for Mn:Zn = 0.025) and 0.45% (for Mn:Zn = 0.05). This linear scaling of Mn concentration in the nanocrystal with Mn:Zn ratio in solution is consistent with an adsorption process characterized by a very high sticking probability, in agreement with the large theoretical Mn binding energies (4–6 eV) for zinc-blende (001) facets.

Both of these Mn:Zn ratios lead to the same doping efficiency, $f = 0.09$, well within the predicted range of allowed doping fraction for ZnSe. For nanocrystals grown using enhanced anion/cation ratios (Se:Zn = 3–4) the measured Mn concentrations were indeed higher, 0.30% (for Mn:Zn = 0.025) and 0.60% (for Mn:Zn = 0.05), a doping efficiency of $f = 0.12$. We attribute this 30% increase in doping efficiency to changes in the equilibrium crystal shape. In other words, by increasing the Se:Zn ratio, the Se chemical potential was raised, which in turn reduced the surface energy of the Se-rich (001) facets, increasing their relative surface area.

In small nanocrystals, photoluminescence spectroscopy provides a more sensitive probe of Mn impurity concentration than ICP. Optically excited Mn-doped ZnSe nanocrystals exhibit two photoluminescence lines, as shown in Fig. 3a. One is due to an internal Mn^{2+} transition, and the other from exciton recombination at the ZnSe band edge. The average number of Mn atoms in the nanocrystal, $\bar{N}$, can be determined from the intensity ratio of these emission lines, I_{Mn}/I_{ZnSe}, while the size of the nanocrystal can be determined from the spectral shift (relative to bulk) of the ZnSe emission line. Hence, we can obtain detailed information about the distribution of Mn within the nanocrystals by analysing how I_{Mn}/I_{ZnSe} varies with $\bar{N}$.

The intensity ratios in Fig. 3b demonstrate that Mn incorporation rises monotonically with increasing Se:Zn ratio, as predicted, for a wide range of nanocrystals. Interestingly, I_{Mn}/I_{ZnSe} falls rapidly to zero for nanocrystals smaller than ~20 Å, suggesting a central core that resists doping. This is not unexpected, since the assumption of a faceted equilibrium shape must eventually break down for small nanocrystals. Indeed, in this size regime many semiconductors form non-crystalline cage-like clusters[26,27], typically with highly stable surfaces that suppress impurity adsorption. Accordingly, we model the distribution of Mn in the nanocrystal as shown in Fig. 3c and d.

The theoretical binding energies of Fig. 1 also suggest that CdSe nanocrystals (which normally have the wurtzite structure) would be easier to dope if they could be grown in the zinc-blende structure. To test this prediction, we grew core/shell nanocrystals in which a shell
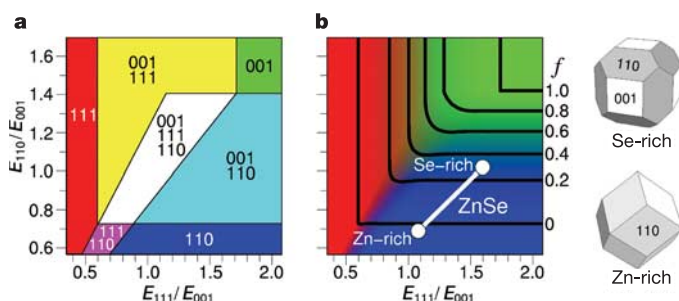
of CdSe was deposited on a ZnSe core[28], as shown in Fig. 4a. Because ZnSe has the zinc-blende structure, the CdSe shell can be expected to adopt this structure. Under certain growth conditions this indeed occurs, as confirmed by the X-ray diffraction data in Fig. 4b. Using these conditions, we grew CdSe shells on undoped ZnSe cores, using a growth solution containing Mn, then used electron paramagnetic resonance (EPR) to determine the location of the Mn (ref. 8). The result, shown in Fig. 4c along with control spectra, shows a six-line spectrum with a hyperfine splitting expected for Mn at lattice sites in cubic CdSe (ref. 29), consistent with the prediction that Mn is more easily incorporated into zinc-blende CdSe.

Finally, we address the role of surfactants in nanocrystal doping. The Mn binding energies shown in Fig. 1 were calculated for clean surfaces. These are relevant energies because during growth, the surfactant molecules detach from the nanocrystal, allowing adsorption onto the clean surface underneath. But the surfactants themselves can also bind Mn, competing with surface adsorption and quenching the doping. This may become important in cases where the Mn–substrate binding is only moderately strong. For example, the binding energy of Mn on the (0001) surface of wurtzite CdSe is two times smaller than on ZnSe(001). This suggests that previous failures to dope CdSe may have resulted not only from intrinsic

properties of CdSe, but also from parasitic binding of Mn by strong surfactants (such as phosphonic acids[30]). It also raises the possibility that the incorporation of Mn into previously undopable wurtzite CdSe nanocrystals may be feasible, although this is likely to be more difficult than in ZnSe.

To examine this possibility, we grew CdSe nanocrystals in the presence of Mn (Mn:Cd = 0.05) under the same surfactant conditions used for ZnSe. According to X-ray diffraction (Fig. 4d) and EPR (Fig. 4e) data, the resulting CdSe nanocrystals have the wurtzite structure and exhibit a hyperfine splitting expected for Mn at hexagonal lattice sites in CdSe (ref. 29). Although this clearly indicates successful doping, ICP measurements also show that the Mn incorporated was only 0.14%, three times less than under identical conditions for ZnSe. We attribute this reduction to the smaller Mn adsorption binding energy, a nanocrystal shape with less adsorbing surface area, or both.

Although we have limited our discussion to II–VI and IV–VI nanocrystals and Mn impurities, the most general formulation of our model—that doping is controlled by impurity adsorption on the nanocrystal surface—provides a framework appropriate for other semiconductor families and impurities as well. For example, III–V
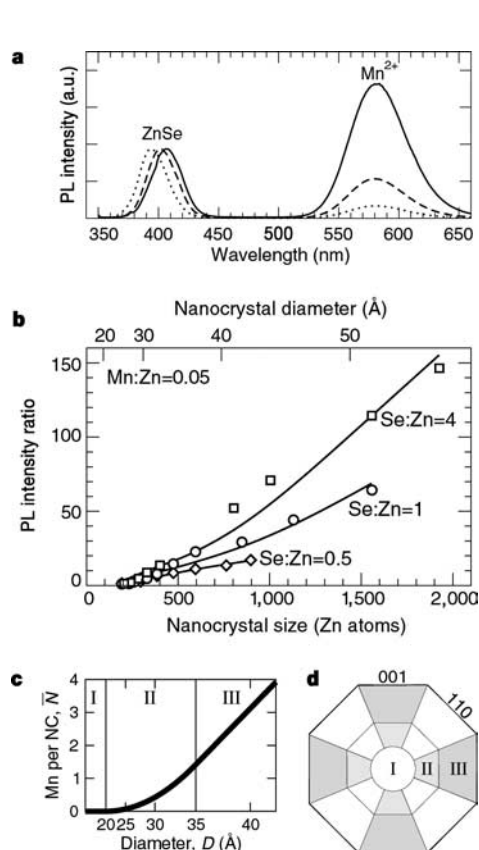

Figure 3 | **Photoluminescence data and theoretical doping model for ZnSe nanocrystals doped with Mn. a**, Typical photoluminescence (PL) spectra for three different nanocrystal sizes[8]. **b**, Dependence of intensity ratios on nanocrystal size for different Se:Zn ratios. Symbols are experimental data; curves are fits to our optical excitation model (see Methods in Supplementary Information). **c**, Model describing radial distribution of Mn incorporated in a nanocrystal: for diameter $D < 20$ Å (region I), no Mn is incorporated; for $D > 35$ Å (region III), every site in the fraction f of the nanocrystal volume is doped with probability x, taken equal to the Mn:Zn ratio in the growth solution; for the transitional region 20 Å $< D < 35$ Å (region II), a smooth interpolation is assumed. For the most favourable doping conditions used, our largest nanocrystals contain on average 12 Mn atoms. NC, nanocrystal. **d**, Cross-sectional view of a schematic nanocrystal, with dopable regions shaded (for clarity, $f = 0.5$ is used in this view).
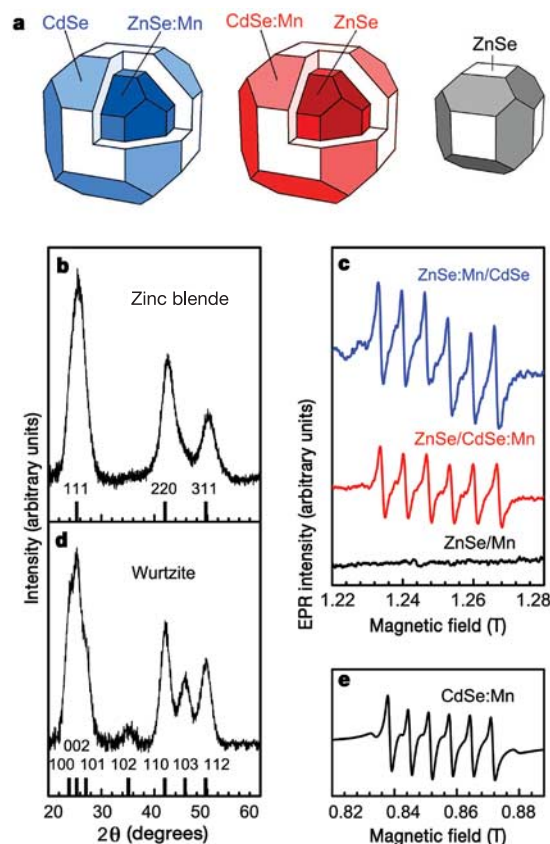

Figure 4 | **Mn doping of zinc-blende and wurtzite CdSe nanocrystals. a**, ZnSe/CdSe:Mn core/shell nanocrystals (red) and two control samples, ZnSe:Mn/CdSe core/shell nanocrystals (blue), and ZnSe nanocrystals heated in the presence of Mn (grey). The latter were grown to rule out the possibility that Mn entered the ZnSe core during the CdSe shell growth. In all three samples, the ZnSe core diameter was 36 Å. **b**, X-ray diffraction pattern for ZnSe/CdSe:Mn core/shell nanocrystals. The expected peak positions for zinc-blende CdSe are indicated. **c**, 35-GHz EPR spectra for the three types of nanocrystals illustrated in **a**. The hyperfine splittings are 65.6 G (blue) and 65.9 G (red). Mn was not detected in the second control sample (black). **d**, X-ray diffraction pattern for CdSe:Mn nanocrystals. The expected peak positions for wurtzite CdSe are indicated. **e**, 24-GHz EPR spectra for the wurtzite CdSe:Mn nanocrystals. The hyperfine splitting is 66.1 G.

and group-IV nanocrystals may, because of their increased covalency, exhibit a variety of surface morphologies quite different from their bulk reconstructions. Nevertheless, those morphologies—if known—can still provide detailed insight into doping. Indeed, for any nanocrystal with well-defined facets, differential adsorption offers a new route to the control of doping. In this way, recent experimental advances in controlling the shape[30] and crystal structure of nanocrystals may also become extremely important in optimizing the efficiency with which the nanocrystals can be doped.

METHODS

Theoretical. Surface energies and Mn–adsorbate binding energies were calculated within density-functional theory in the generalized-gradient approximation[23], using the projector-augmented-wave method as implemented in VASP[22]. Surfaces were represented by eight-layer (or thicker) slabs with the theoretical equilibrium lattice constant, reconstructed on one side and appropriately passivated on the other. Surface reconstructions from the literature were used when available; otherwise, separate studies were performed to establish the lowest-energy reconstruction from a pool of likely candidates (see discussion in Supplementary Information). Full atomic relaxation was performed for all but the bottom semiconductor layer, using 4×4 sampling of the surface Brillouin zone. For the (spin-polarized) adsorbate calculations, 2×2 supercells were used to represent isolated Mn adsorbates; within this cell, binding energies (using 2×2 sampling) at different adsorption sites were compared and the largest value reported. For surfaces that have more than one stable reconstruction within the allowed range of chemical potential, Mn binding energies are reported for the anion-rich reconstruction. Absolute surface energies for ZnSe(001) and (110) were computed using symmetric slabs. For the inequivalent (111)A and B orientations this is not possible, so we approximated the (111)A and B surface energies by their average. (See the discussion in Supplementary Information for details about the ZnSe reconstructions.) The Se- and Zn-rich limits of the chemical potential were defined by the Se (A8) phase of Se and the hexagonal close-packed phase of Zn, respectively.

Experimental. Mn-doped ZnSe nanocrystals were synthesized as previously reported[8]. To change the ratio of Se to Zn in the reaction, the number of moles of each was adjusted while constraining the total number of moles. The amount of Mn added was relative to the Zn concentration. To obtain the largest nanocrystals, additional precursors (in the same ratios) were sometimes added to avoid saturation in the growth. CdSe shells were deposited on ZnSe cores by modifying the procedure of ref. 28. First, ZnSe cores were prepared by injecting 4 ml of trioctylphosphine (TOP), 1 ml of 1-M Se in TOP, and 82 μl of diethylzinc into 10 ml of distilled and degassed hexadecylamine (HDA) at 310 °C. (For Mn-doped ZnSe cores, 1.0 ml of 0.04-M dimethylmanganese in a tetrahydrofuran/toluene mixture[8] was included in the injection.) The mixture was then heated at 260–300 °C until the first absorption peak was at 400 nm. To coat with CdSe, 3 ml of this solution was combined with 6 ml of distilled and degassed HDA and heated to 270 °C, followed by dropwise addition (over 30 min) of a mixture of 45 μl of dimethylcadmium, 2.4 ml of 1-M Se in TOP, and 4 ml of TOP. (For Mn-doped CdSe shells, 0.75 ml of 0.04-M dimethylmanganese was included in the addition. For the second control sample, the addition included only 0.75 ml of 0.04-M dimethylmanganese and 2 ml of TOP.) Afterwards, the solution was stirred at 150 °C for 24 h. Mn-doped CdSe nanocrystals were obtained by injecting 4 ml of TOP, 0.8 ml of 1-M Se in TOP, 60 μl of dimethylcadmium, and 1.0 ml of freshly prepared 0.04-M dimethylmanganese into 12 ml of distilled and degassed HDA at 300 °C. The mixture was then heated at 270 °C until the first absorption peak reached 600 nm. Owing to the weak binding of HDA, the CdSe nanocrystals easily formed aggregates.

Before characterization with ICP and EPR, all samples were precipitated and repeatedly washed with pyridine[8,12] to remove excess Mn at the particle surface, as confirmed by EPR. ICP was performed on a Perkin-Elmer Optima 3000DV after dissolving the nanocrystals in aqua regia. Photoluminescence was collected with a Spex Fluorolog-2 spectrofluorometer. X-ray diffraction was measured with a Panalytics X'Pert diffractometer using Cu K radiation at 45 kV and 40 mA after the nanocrystals had been precipitated three times with methanol, dispersed in 10% octane in hexane, and then spin-coated onto silicon wafers. For EPR, the nanocrystals were cast in poly(lauryl methacrylate) films or collected as a powder. Room temperature spectra were measured at 35 and 24 GHz.

1. Ekimov, A. I. & Onushchenko, A. A. Quantum size effect in 3-dimensional microscopic semiconductor crystals. *JETP Lett.* **34**, 345–349 (1981).
2. Efros, Al. L. & Efros, A. L. Interband absorption of light in a semiconductor sphere. *Sov. Phys. Semicond.* **16**, 772–775 (1982).
3. Brus, L. E. A simple model for the ionization potential, electron affinity, and aqueous redox potentials of small semiconductor crystallites. *J. Chem. Phys.* **79**, 5566–5571 (1983).
4. Alivisatos, A. P. Semiconductor clusters, nanocrystals, and quantum dots. *Science* **271**, 933–937 (1996).
5. Wang, Y., Herron, N., Moller, K. & Bein, T. 3-dimensionally confined diluted magnetic semiconductor clusters: $Zn_{1-x}Mn_xS$. *Solid State Commun.* **77**, 33–38 (1991).
6. Bhargava, R. N., Gallagher, D., Hong, X. & Nurmikko, A. Optical properties of manganese-doped nanocrystals of ZnS. *Phys. Rev. Lett.* **72**, 416–419 (1994).
7. Levy, L., Hochepied, J. F. & Pileni, M. P. Control of the size and composition of three dimensional diluted magnetic semiconductor clusters. *J. Phys. Chem.* **100**, 18322–18326 (1996).
8. Norris, D. J., Yao, N., Charnock, F. T. & Kennedy, T. A. High-quality manganese-doped ZnSe nanocrystals. *Nano Lett.* **1**, 3–7 (2001).
9. Suyver, J. F., Wuister, S. F., Kelly, J. J. & Meijerink, A. Luminescence of nanocrystalline ZnSe:Mn^{2+}. *Phys. Chem. Chem. Phys.* **2**, 5445–5448 (2000).
10. Hanif, K. M., Meulenberg, R. W. & Strouse, G. F. Magnetic ordering in doped $Cd_{1-x}Co_xSe$ diluted magnetic quantum dots. *J. Am. Chem. Soc.* **124**, 11495–11502 (2002).
11. Stowell, C. A., Wiacek, R. J., Saunders, A. E. & Korgel, B. A. Synthesis and characterization of dilute magnetic semiconductor manganese-doped indium arsenide nanocrystals. *Nano Lett.* **3**, 1441–1447 (2003).
12. Mikulec, F. V. et al. Organometallic synthesis and spectroscopic characterization of manganese-doped CdSe nanocrystals. *J. Am. Chem. Soc.* **122**, 2532–2540 (2000).
13. Shim, M. & Guyot-Sionnest, P. n-type colloidal semiconductor nanocrystals. *Nature* **407**, 981–983 (2000).
14. Hoffman, D. M. et al. Giant internal magnetic fields in Mn doped nanocrystal quantum dots. *Solid State Commun.* **114**, 547–550 (2000).
15. Efros, Al. L., Rashba, E. I. & Rosen, M. Paramagnetic ion-doped nanocrystal as a voltage-controlled spin filter. *Phys. Rev. Lett.* **87**, 206601 (2001).
16. Huynh, W. U., Dittmer, J. J. & Alivisatos, A. P. Hybrid nanorod-polymer solar cells. *Science* **295**, 2425–2427 (2002).
17. Wolf, S. A. et al. Spintronics: a spin-based electronics vision for the future. *Science* **294**, 1488–1495 (2001).
18. Hwang, I. S., Kim, H. D., Kim, J. E., Park, H. Y. & Lim, H. Solid solubilities of magnetic ions in diluted magnetic semiconductors grown under equilibrium conditions. *Phys. Rev. B* **50**, 8849–8852 (1994).
19. Jamil, N. Y. & Shaw, D. The diffusion of Mn in CdTe. *Semicond. Sci. Technol.* **10**, 952–958 (1995).
20. Shiang, J. J., Kadavanich, A. V., Grubbs, R. K. & Alivisatos, A. P. Symmetry of annealed wurtzite CdSe nanocrystals — assignment to the C_{3v} point group. *J. Phys. Chem.* **99**, 17417–17422 (1995).
21. Peng, X. G., Wickham, J. & Alivisatos, A. P. Kinetics of II–VI and III–V colloidal semiconductor nanocrystal growth: 'Focusing' of size distributions. *J. Am. Chem. Soc.* **120**, 5343–5344 (1998).
22. Kresse, G. & Furthmuller, J. Efficient iterative schemes for ab initio total-energy calculations using a plane-wave basis set. *Phys. Rev. B* **54**, 11169–11186 (1996).
23. Perdew, J. P., Burke, K. & Ernzerhof, M. Generalized gradient approximation made simple. *Phys. Rev. Lett.* **77**, 3865–3868 (1996).
24. Ji, T. H., Jian, W. B. & Fang, J. Y. The first synthesis of $Pb_{1-x}Mn_xSe$ nanocrystals. *J. Am. Chem. Soc.* **125**, 8448–8449 (2003).
25. Wortis, M. *Chemistry and Physics of Solid Surfaces VII* Ch. 13 (Springer, Berlin, 1988).
26. Kasuya, A. et al. Ultra-stable nanoparticles of CdSe revealed from mass spectrometry. *Nature Mater.* **3**, 99–102 (2004).
27. Kaxiras, E. Effect of surface reconstruction on stability and reactivity of Si clusters. *Phys. Rev. Lett.* **64**, 551–554 (1990).
28. Balet, L. P., Ivanov, S. A., Piryatinski, A., Achermann, M. & Klimov, V. I. Inverted core/shell nanocrystals continuously tunable between type-I and type-II localization regimes. *Nano Lett.* **4**, 1485–1488 (2004).
29. Koh, A. K. & Miller, D. J. The systematic variation of the EPR parameters of manganese in II–VI semiconductors. *Solid State Commun.* **60**, 217–222 (1986).
30. Peng, X. G. et al. Shape control of CdSe nanocrystals. *Nature* **404**, 59–61 (2000).

Author Information Reprints and permissions information is available at npg.nature.com/reprintsandpermissions. The authors declare no competing financial interests. Correspondence and requests for materials should be addressed to S.C.E. (Steven.Erwin@nrl.navy.mil) or D.J.N. (dnorris@umn.edu).